Science Advances
AAAS

Supplementary Materials for

Electric field control of perpendicular magnetic tunnel junctions with easy-cone magnetic anisotropic free layers

Weideng Sun *et al.*

Corresponding author: Weisheng Zhao, weisheng.zhao@buaa.edu.cn; Yonggang Zhao, ygzhao@tsinghua.edu.cn

Sci. Adv. **10**, eadj8379 (2024)
DOI: 10.1126/sciadv.adj8379

This PDF file includes:

Supplementary Text

S1. *m-H* loop of the MTJ multilayer stack and *R-H* curve of the MTJ pillar

Magnetic moments in the MTJ can be divided into three sections as shown in the inset of Fig. S1A including the FL composed of two ferromagnetically coupled CoFeB layers through a 0.3 nm W spacer (red), the RL CoFeB with compensatory layer Co and one part of SAF structure (green), the other part of SAF structure (blue). Figure S1A is the *m-H* loop of the MTJ multilayer stack and the magnetic moment directions of the three sections are shown for the different stages. In principle, the magnetic moments in the RL (green and blue sections) should be cancelled out (*51*). And the magnitudes of the magnetic moments in CoFeB/W/Co and $(Co/Pt)_3$ should be comparable. The Co/Pt multilayer structures possess strong PMA, so the reversal of magnetic moment at about ±3100 Oe reflects the complete switching of $(Co/Pt)_6$ (1.78×10^{-4} emu). Owing to the easy-cone state of the FL, the magnetic moment changes slowly at low magnetic fields and the coercive field should be very small. The obvious coercive field and residual magnetic moment (about 2×10^{-5} emu) result from the nonideal magnetic moment alignment of the CoFeB/W/Co as discussed later.

Figure S1B is the *R-H* curve of the MTJ pillar (10 μm diameter). The TMR ratio is about 74% according to the maximum and minimum resistance values. The *R-H* curve shows some fine structures (peaks and dips) within ±1000 Oe and can be understood by considering the variations of the FL and the nonideal RL with magnetic field.

S2. Variation of the magnetic properties of the RL with the magnetic field

In order to investigate the switching behavior of the RL with magnetic field, a multilayer stack without the FL section was deposited and characterized. In principle, the magnetic moment of the RL should remain almost unchanged during the measurement of the minor *m-H* loop (±2000 Oe) because of its large switching field (beyond 2000 Oe) as shown in Fig. S1A. However, the variation of magnetic moment is 1.82×10^{-5} emu between +2000 and -2000 Oe (Fig. S2A), accounting for about 17% of the total magnetic moment of the RL. It's worth noting that only the ferromagnetically coupled layers CoFeB/W/Co contribute to this variation as shown in the bottom inset of Fig. S2A, while the magnetic moments of Co/Pt multilayers remain almost unchanged because of the strong PMA. The alignments of magnetic moments of CoFeB/W/Co may become nonideal for some regions of the junctions and this nonideality may be related to the growth quality of the multilayer stacks in the Co/Ta/$(Co/Pt)_3$ ferromagnetically coupled structures, where some defects may exist owing to the very thin Ta spacer layer resulting in decoupling between Co and $(Co/Pt)_3$, as illustrated by the thick blue (normal magnetic moment alignment in RL) and thin orange (nonideal magnetic moment alignment in RL) arrows in the bottom inset of Fig. S2A. This can account for the angular dependence of TMR (S3).

As shown in the top inset of Fig. S2A, when the magnetic field decreases from +20000 Oe, the magnetic moments of the ferromagnetically coupled CoFeB/W/Co/Ta/$(Co/Pt)_3$ layers switch downward firstly at about +2500 Oe, because the magnetic field is not strong enough to overcome the antiferromagnetic coupling between the $(Co/Pt)_6$ and the coupled layers. The magnetic moment of $(Co/Pt)_6$ switches downward at about -4000 Oe (top inset of Fig. S2A). While for the nonideal regions, because of the decoupling between Co and $(Co/Pt)_3$, the magnetic moments of CoFeB/W/Co do not change with the variation of $(Co/Pt)_3$, and change with magnetic field instead. The nonideal regions gradually decrease with magnetic field sweeping from +20000 to -20000 Oe, which means that the relative portions of the regions with magnetic moments upward (nonideal) or downward (normal) change with magnetic field and induce some fine structures in the *R-H* curve. Besides, the minor *m-H* loop is not symmetric with respect to the origin of *m* because the reversal of magnetic moments of CoFeB+Co is incomplete. In fact, the RL possesses perpendicular magnetic moment without in-plane magnetic component.

As we can see from the out-of-plane *m-H* curve of the MTJ multilayer stack (Fig. S1A), the *m* related to the $(Co/Pt)_6$ layer (blue arrows in the inset of Fig. S1A) switches sharply above 3 kOe with the out-of-plane magnetic field sweeping from -7 to +7 kOe. Meanwhile, the $(Co/Pt)_6$ layer has strong antiferromagnetic exchange interaction on the CoFeB+Co+$(Co/Pt)_3$ layer (green arrows in the inset of Fig. S1A), which switches downward above 2 kOe with the out-of-plane magnetic field decreasing from +7 kOe. However, from the in-plane *m-H* curve of the RL sample (Fig. S2B), the remanent *m* is close to zero, and the *m* changes slowly under in-plane magnetic fields, which shows the hard axis property. The results indicate that our RL corresponds to PMA.

S3. Angular dependence of TMR

For MTJ, the Slonczewski model gives an expression of the tunnel conductance as follows (*56, 73*):

$$G(\varphi) = G_0(1 + P^2 \cos\varphi) \quad (1)$$

where G_0 is a coefficient; P is the spin polarization at Fermi level E_F relying on the FM layers; φ is the angle between the magnetic moment directions in the two FM electrodes. From formula

(1), the resistance is then given by

$$R(\varphi) = \frac{R_0}{1 + P^2 \cos\varphi} \tag{2}$$

where R_0 is a coefficient. Particularly, considering two conditions where the magnetization configurations of two CoFeB layers are parallel (P) and antiparallel (AP) states corresponding to φ with 0° and 180°, respectively, one can get the following:

$$\begin{aligned} R_{\mathbf{P}} &= \frac{R_0}{1+P^2} \\ R_{\mathbf{AP}} &= \frac{R_0}{1-P^2} \end{aligned} \tag{3}$$

From Fig. 3B, R_P = 75.07 ohm, R_{AP} = 140.67 ohm; then we can get

$$\begin{aligned} & R_0 = 97.9 \\ & P^2 = 0.304 \\ & \varphi = \arccos(\frac{97.9 / R(\varphi) - 1}{0.304}) \end{aligned} \tag{4}$$

At the same time, the easy-cone angle θ can be calculated as $\theta = 180° - \varphi$. Thus, the change of θ can be deduced form the change of φ.

According to the angular dependence of TMR, we can calculate the tunnel resistance at 0 Oe (presetting at +2000 Oe) by analyzing the residual magnetic moment of the *m-H* loop (Fig. S1A) that results from the nonideal regions in the RL (1×10^{-5} emu at 0 Oe). The magnetic moment of $(Co/Pt)_6$ is deduced from Fig. S1A about 8.9×10^{-5} emu, so the ratio of the nonideal regions accounts for about 22.5% of the total magnetic moments of CoFeB/W/Co. The easy-cone angle of the FL in an unpoled state is about 40° (Fig. 1B). When the angle between the FL and RL is 40° (corresponding to the nonideal regions in the RL), the tunneling resistance is about 352.9 ohm. When the angle between the FL and RL is 140° (corresponding to the normal regions in the RL), the tunneling resistance is about 164.7 ohm. The total resistance should be the parallel value of the two resistance channels corresponding to 112.3 ohm, which is consistent with the experimental value (about 109 ohm at 0 Oe in Fig. 2A).

S4. Larger modulation in another MTJ pillar and MTJ device damage by the electrostatic effect

In our experiment, one MTJ pillar shows a larger modulation as shown in Fig. S3A. The overall *R*-*H* behavior is similar to that in Fig. 3B. The *R*-*E* curve at +600 Oe after presetting at +2000 Oe is shown in Fig. S3B. A larger modulation of resistance (33%) is realized at +0 and -0 kV/cm (red and blue squares), which means that the performance can be improved if the design and processing of MTJ are optimized. Similar to the calculation method for Fig. 3D, the change of the easy-cone angle $\Delta\theta$ derived from the *R*-*E* curve (Fig. S3B) is shown in Fig. S3C by selecting $\Delta\theta = 0°$ for -0 kV/cm (blue square). The change of nonvolatile easy-cone angle is calculated to be about 50° at +0 kV/cm (red square in Fig. S3C). Schematic illustration (Fig. S3D) also shows the modulation of easy-cone state of the FL under ±0 kV/cm (red and blue circular conical surfaces and arrows). However, the MTJ device is damaged due to the electrode broken induced by the electrostatic effect, which can induce the open circuit or poor connection during the electrical transport measurement. In this case, the MTJ resistance can become very large. The corresponding experimental result is shown in Fig. S3, E and F.

The electrostatic effect can also exist during the electrical transport measurement or the process of sample transfer. Thus, electric breakdown of the MgO barrier of the MTJ device may occur occasionally and the MTJ resistance can be much smaller than the normal tunneling resistance (70 ~ 140 Ω), the experimental results of some typical devices are as shown in Fig. S3, G and H.

The electrostatic effect can be effectively avoided by wearing an electrostatic bracelet, keeping ground connection of the electrodes, and increasing air humidity during the electrical measurement, etc.

S5. *P-E* loop of PMN-PT

The *P-E* loop of PMN-PT is shown in Fig. S5. The coercive field is about 2 kV/cm, which is consistent with the previous report (*74*) and the switching field of the *R-E* curves (Fig. 3C).

S6. LRSM for the (222) reflection with in situ electric fields

The LRSM for the (222) reflection of PMN-PT beneath the MTJ pillar was performed with in situ electric fields (+10 → -10 → +10 kV/cm) through X-ray microdiffraction, and the results are shown in Fig. S6. From +10 to +0 kV/cm (A to D), there only exists one diffraction spot. After -1 kV/cm, two spots appear near the coercive field of PMN-PT (E to G) and remain almost unchanged (H to M) even at -0 kV/cm (L). After +1.5 kV/cm, two spots gradually change to one spot near the coercive field of PMN-PT (N to P) and this spot keeps almost unchanged (Q and R). The variation of the diffraction spots means that there exists FE phase transition under different electric fields and the transition is nonvolatile, which induces the nonvolatile modulation behavior of the resistance.

S7. Interplanar spacings of the (222) reflection under different electric fields

The interplanar spacings deduced from the X-ray microdiffraction results (Fig. S6) under different electric fields are shown in Fig. S7A. There exists one diffraction spot (black circle) at positive polarization, while two spots named big spot (red circle) and small spot (blue circle) according to the diffraction intensity at negative polarization. The splitting of the spots reflects different FE phases in PMN-PT.

Spontaneous polarizations of PMN-PT with the R and O phases in the (011)-cut case and the position of (222) crystal face are shown in Fig. S7B. The in-plane main axes are the [100] and [01-1] directions corresponding to x and y, respectively. The cubic lattice axes [100], [010], [001] are also shown.

S8. Local strain along the [111] crystal orientation

According to the lattice parameters of R phase of PMN-PT (lattice structure in Fig. S7B), the interplanar spacing for the (hkl) reflection can be calculated by the following formula (*75*)

$$\frac{1}{d_{hkl}^2} = \frac{(h^2+k^2+l^2)\sin^2\alpha + 2(hk+hl+kl)(\cos^2\alpha - \cos\alpha)}{a^2(1-3\cos^2\alpha + 2\cos^3\alpha)} \tag{5}$$

where d_{hkl} is the interplanar spacing with the Miller indices hkl; a and α are the lattice parameters of R phase of PMN-PT. For the (222) crystal face, $h = k = l = 2$. And using a = 0.4017 nm, α = 89.89° (*63*), d_{222} can be calculated to be 0.11618 nm.

Considering the big spot (Fig. S7A) reflects the R-O phase transition, the local strain along the [111] crystal orientation was calculated using the big spot

$$Strain = \frac{d_E - d_{222}}{d_{222}} \times 100\% \tag{6}$$

where d_E is the interplanar spacing of the (222) reflection corresponding to the big spot under different electric fields (Fig. S7A); d_{222} with 0.11618 nm is selected as the reference point. And the result is shown in Fig. 4E.

S9. Evolution of PMN-PT (022) diffraction peak with in situ electric field

To characterize the evolution of the (022) diffraction peak (lattice change along the OOP direction) of PMN-PT, XRD with in situ electric field was performed. And the result is shown in Fig. S8. The electric field sweeps with +10 → -10 → +10 kV/cm as indicated by the pink arrows. The dashed grey lines pass the larger peak (reflecting the trend of lattice change) under different electric fields in order to calculate the (022) interplanar spacing. According to the Bragg diffraction formula $2d\sin\theta = n\lambda$ and the lattice parameters of R phase of PMN-PT (details in S8), the macroscopic strain along the [011] crystal orientation with in situ electric field was obtained as shown in Fig. 4F.

S10. Strain properties of PMN-PT along the in-plane [100] and [01-1] crystal orientations

The strain versus electric field curve measured by strain gauges along the in-plane [100] crystal orientation is shown in Fig. S10A. It is different from the butterfly-like strain behavior generally observed (*44, 66*), and shows large compressive strains for negative electric fields.

The strain curve along the in-plane [01-1] crystal orientation is shown in Fig. S10B. There exist two peaks near the coercive field of PMN-PT. It is also different from the strain behavior for the general case (*44, 66*). And more importantly, there exist nonvolatile residual strains at ±0 kV/cm, which can be the origin of the nonvolatile modulation of the resistance state.

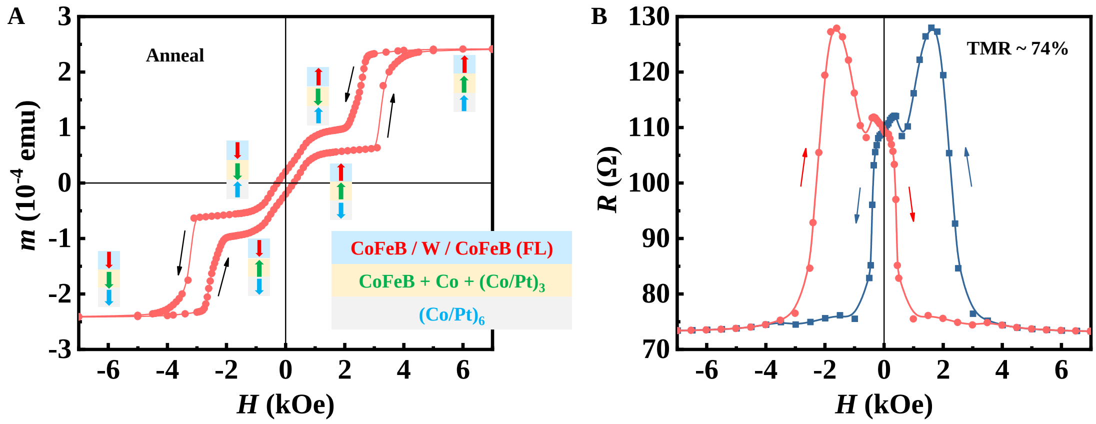

Fig. S1. *m-H* loop of the MTJ multilayer stack and *R-H* curve of the MTJ pillar. (A) *m-H* loop and magnetic moment directions of the three sections in the MTJ multilayer stack. The black arrows represent the sweeping direction of magnetic field. **(B)** *R-H* curve of the MTJ pillar. The blue and red arrows represent the sweeping directions of magnetic field.

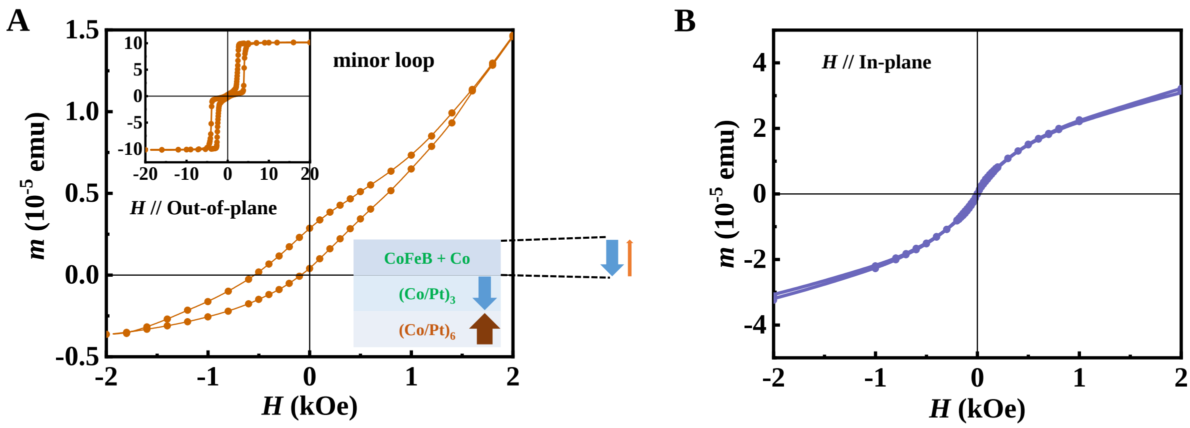

Fig. S2. Out-of-plane and in-plane *m-H* loop of the multilayer stack without the FL section. **(A)** Out-of-plane *m-H* loop. Minor *m-H* loop between +2000 and -2000 Oe after presetting at +20000 Oe. The top and bottom insets correspond to the *m-H* loop between +20000 and -20000 Oe and the structure of the multilayer stack, respectively. The magnetic moment alignments of the normal and nonideal regions are illustrated by the blue and orange arrows, respectively. The magnetic moment alignments of the Co/Pt multilayers are also shown. **(B)** In-plane *m-H* loop.

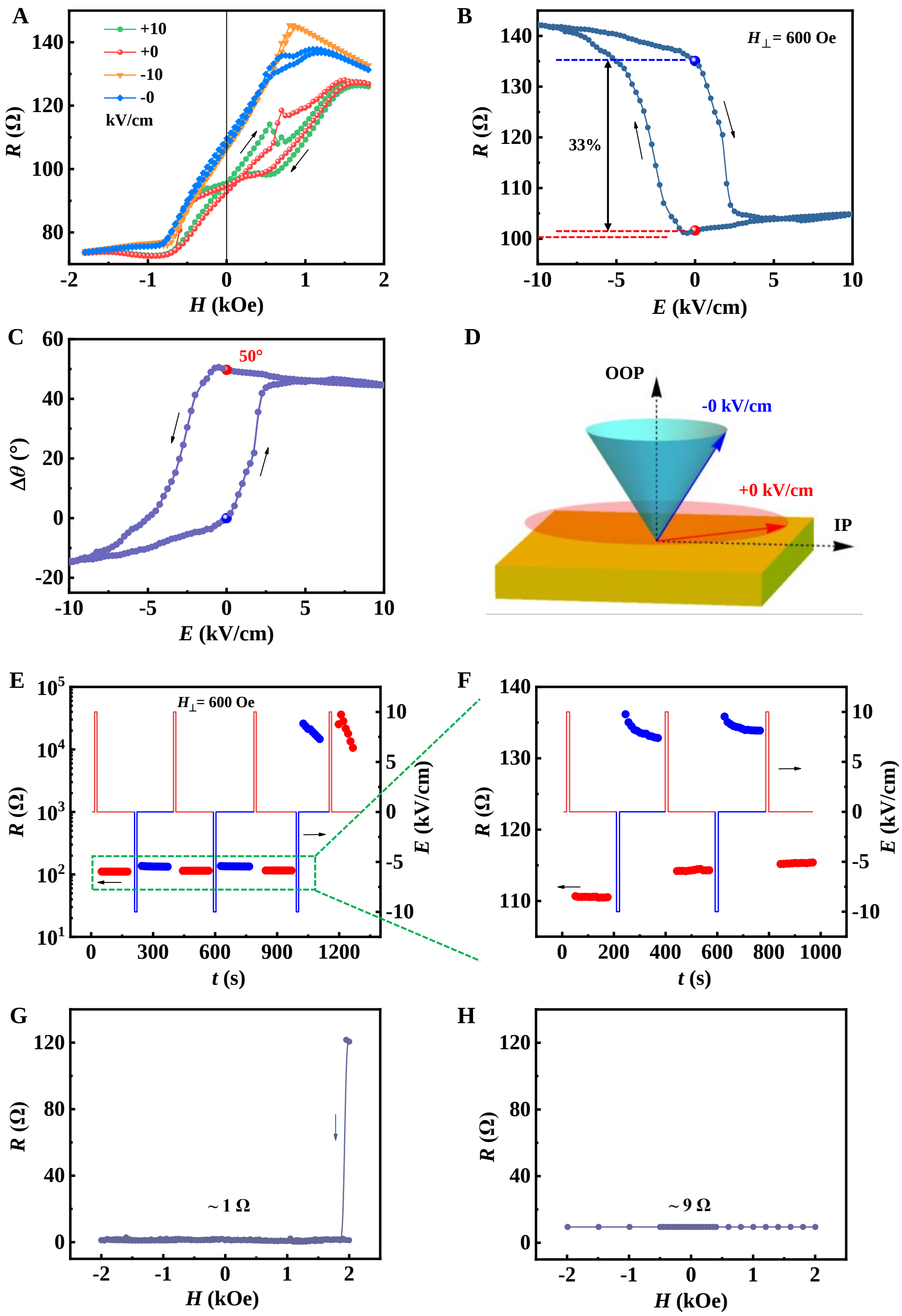

Fig. S3. Larger modulation in another MTJ pillar and MTJ device damage by the electrostatic effect. (A) *R*-*H* curves under different electric fields after presetting at +7000 Oe. The black arrows represent the sweeping direction of magnetic field. **(B)** *R*-*E* curve at +600 Oe after presetting at +2000 Oe. The black arrows represent the sweeping direction of electric field.

The nonvolatile modulation of resistance about 33% is realized at ±0 kV/cm. **(C)** Variation of the easy-cone angle $\Delta\theta$ versus electric field. The values of $\Delta\theta$ at -0 and +0 kV/cm are indicated by the blue and red squares, respectively. The black arrows represent the sweeping direction of electric field. **(D)** Schematic illustrating the modulation of easy-cone state of the FL under ±0 kV/cm, respectively. **(E)** Repeatable bistable resistance states switched by the pulsed electric fields and the damage related to the electrode broken. **(F)** Enlarged portion in **(E)** marked by dashed green box. Nonvolatile resistance induced by electric-field pulses before the device damaged. **(G)**, **(H)** Device damage related to the electric breakdown of MgO.

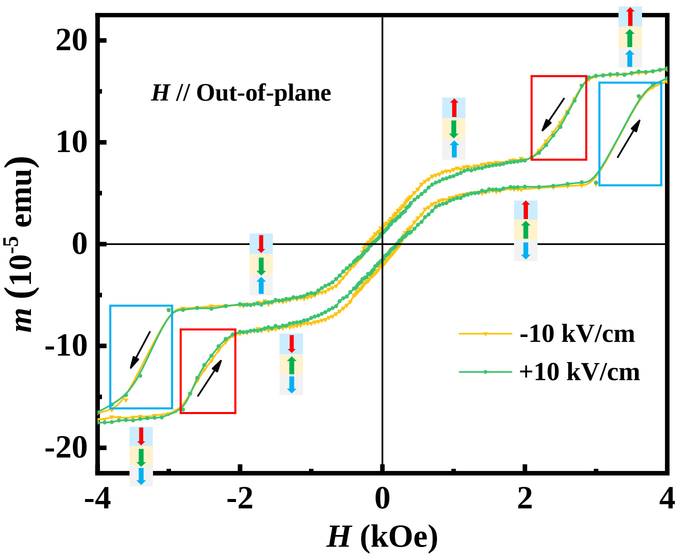

Fig. S4. Out-of-plane *m-H* loops and magnetic moment directions of different functional layers for the MTJ multilayer stack under ±10 kV/cm. The magnetic moment of the RL shows negligible changes with electric fields as indicated by the red and blue squares corresponding to the switching of CoFeB+Co+$(Co/Pt)_3$ and $(Co/Pt)_6$ layer, respectively.

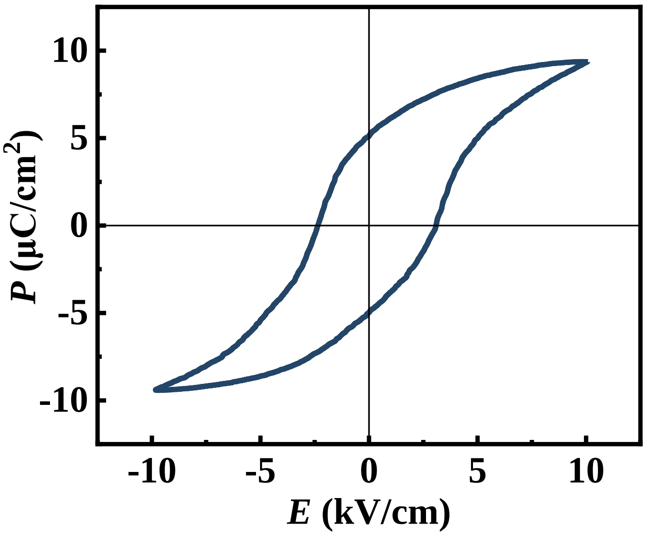

Fig. S5. ***P-E*** **loop of PMN-PT.** The coercive field is about 2 kV/cm.

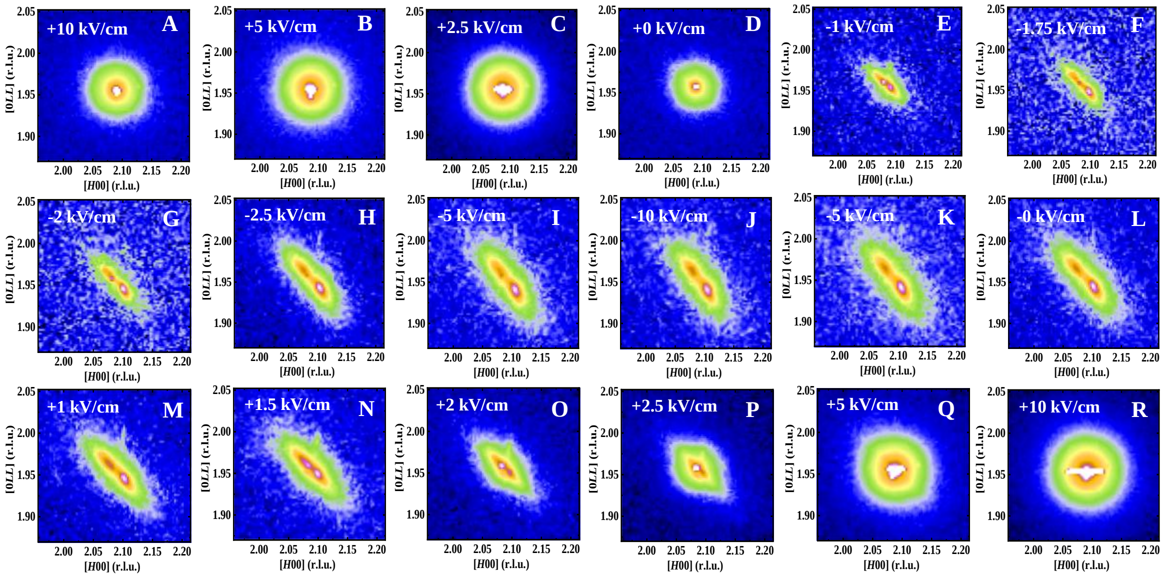

Fig. S6. LRSM for the (222) reflection of PMN-PT beneath the MTJ pillar. Intensity scale runs from blue (low) to white (high) in **(A)**-**(R)**. The white area in the center of the spots is caused by over exposure of the synchrotron radiation X-ray source.

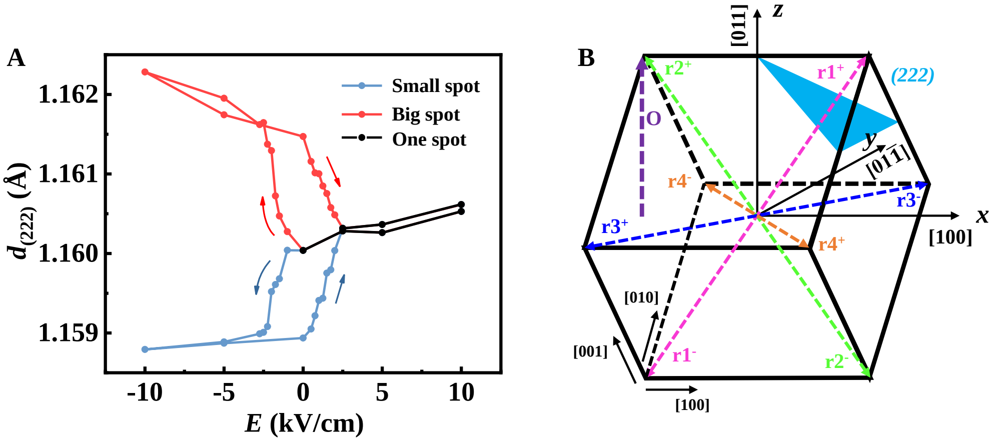

Fig. S7. Interplanar spacings of the (222) reflection and polarizations of PMN-PT. (A) Interplanar spacings of the (222) reflection under different electric fields. The red and blue arrows represent the sweeping directions of electric field. **(B)** Spontaneous polarizations and (222) crystal face of PMN-PT.

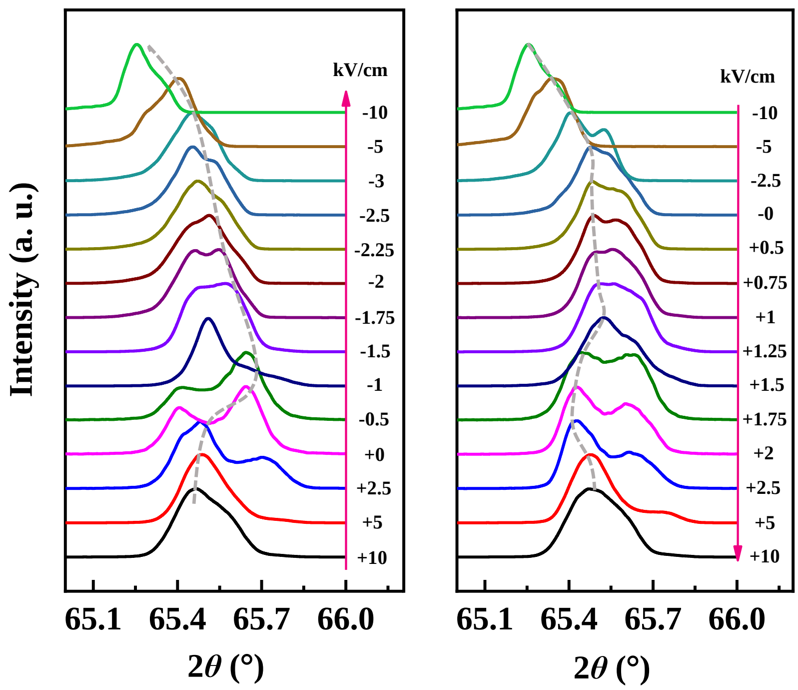

Fig. S8. Evolution of the PMN-PT (022) diffraction peaks with in situ electric field. The pink arrows represent the sweeping direction of the electric field.

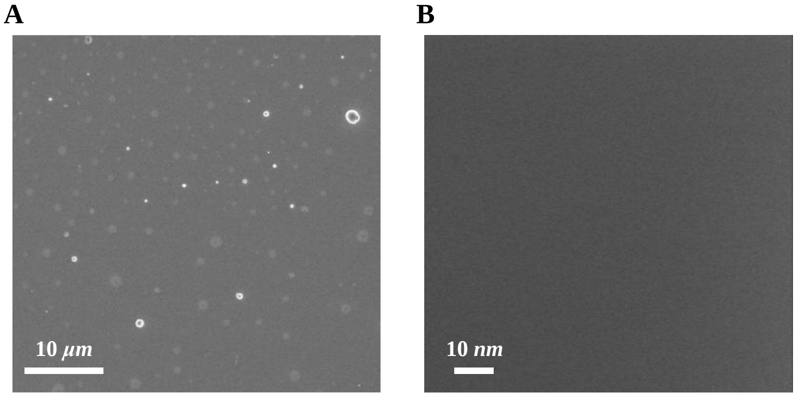

Fig. S9. SEM images of the MTJ multilayer stack for the -0 kV/cm state with different magnifications. (A) and **(B)** show no evident microcracks. White dots are dusts adhered to the surface.

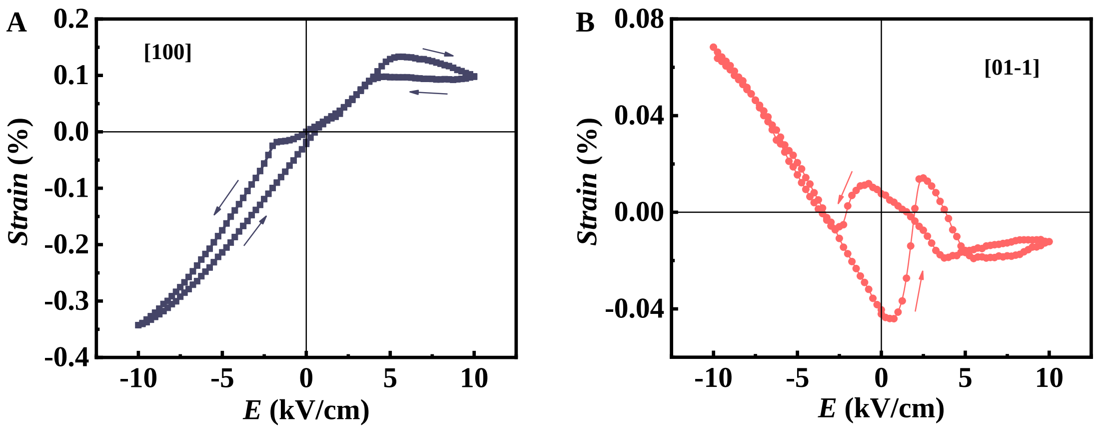

Fig. S10. In-plane strain properties of PMN-PT. Strain properties along the **(A)** in-plane [100] and **(B)** [01-1] crystal orientations, respectively. Black and red arrows represent the sweeping direction of electric field.

REFERENCES AND NOTES

1. S. Tehrani, J. M. Slaughter, M. Deherrera, B. N. Engel, N. D. Rizzo, J. Salter, M. Durlam, R. W. Dave, J. Janesky, B. Butcher, K. Smith, G. Grynkewich, Magnetoresistive random access memory using magnetic tunnel junctions. *Proc. IEEE* **91,** 703–714 (2003).

2. C. Chappert, A. Fert, F. N. Van Dau, The emergence of spin electronics in data storage. *Nat. Mater.* **6,** 813–823 (2007).

3. B. Dieny, I. L. Prejbeanu, Magnetic random-access memory, in *Introduction to Magnetic Random-Access Memory*, B. Dieny, R. B. Goldfarb, K. J. Lee, Eds. (Wiley, 2017), chap. 5.

4. J. Åkerman, Toward a universal memory. *Science* **308**, 508–510 (2005).

5. A. Brataas, A. D. Kent, H. Ohno, Current-induced torques in magnetic materials. *Nat. Mater.* **11**, 372–381 (2012).

6. S. Ikeda, K. Miura, H. Yamamoto, K. Mizunuma, H. D. Gan, M. Endo, S. Kanai, J. Hayakawa, F. Matsukura, H. Ohno, A perpendicular-anisotropy CoFeB-MgO magnetic tunnel junction. *Nat. Mater.* **9,** 721–724 (2010).

7. M. X. Wang, W. L. Cai, D. Q. Zhu, Z. H. Wang, J. Kan, Z. Y. Zhao, K. H. Cao, Z. L. Wang, Y. G. Zhang, T. R. Zhang, C. Park, J. P. Wang, A. Fert, W. S. Zhao, Field-free switching of a perpendicular magnetic tunnel junction through the interplay of spin-orbit and spin-transfer torques. *Nat. Electron.* **1**, 582–588 (2018).

8. L. Q. Liu, C. F. Pai, Y. Li, H. W. Tseng, D. C. Ralph, R. A. Buhrman, Spin-torque switching with the giant spin Hall effect of tantalum. *Science* **336**, 555–558 (2012).

9. N. Sato, F. Xue, R. M. White, C. Bi, S. X. Wang, Two-terminal spin-orbit torque magnetoresistive random access memory. *Nat. Electron.* **1**, 508–511 (2018).

10. I. M. Miron, K. Garello, G. Gaudin, P. J. Zermatten, M. V. Costache, S. Auffret, S. Bandiera, B. Rodmacq, A. Schuhl, P. Gambardella, Perpendicular switching of a single ferromagnetic layer induced by in-plane current injection. *Nature* **476**, 189–193 (2011).

11. I. M. Miron, G. Gaudin, S. Auffret, B. Rodmacq, A. Schuhl, S. Pizzini, J. Vogel, P. Gambardella, Current-driven spin torque induced by the Rashba effect in a ferromagnetic metal layer. *Nat. Mater.* **9**, 230–234 (2010).

12. J. M. Hu, C. W. Nan, Opportunities and challenges for magnetoelectric devices. *APL Mater.* **7**, 080905 (2019).

13. M. Bibes, A. Barthélémy, Multiferroics: Towards a magnetoelectric memory. *Nat. Mater.* **7**, 425–426 (2008).

14. W. G. Wang, M. G. Li, S. Hageman, C. L. Chien, Electric-field-assisted switching in magnetic tunnel junctions. *Nat. Mater.* **11**, 64–68 (2012).

15. Y. Shiota, T. Nozaki, F. Bonell, S. Murakami, T. Shinjo, Y. Suzuki, Induction of coherent magnetization switching in a few atomic layers of FeCo using voltage pulses. *Nat. Mater.* **11**, 39–43 (2012).

16. S. Fusil, V. Garcia, A. Barthélémy, M. Bibes, Magnetoelectric devices for spintronics. *Annu. Rev. Mat. Res.* **44**, 91–116 (2014).

17. Y. X. Shao, V. Lopez-Dominguez, N. Davila, Q. L. Sun, N. Kioussis, J. A. Katine, P. K. Amiri, Sub-volt switching of nanoscale voltage-controlled perpendicular magnetic tunnel junctions. *Commun. Mater.* **3**, 87 (2022).

18. T. Newhouse-Illige, Y. H. Liu, M. Xu, D. R. Hickey, A. Kundu, H. Almasi, C. Bi, X. Wang, J. W. Freeland, D. J. Keavney, C. J. Sun, Y. H. Xu, M. Rosales, X. M. Cheng, S. F. Zhang, K. A. Mkhoyan, W. G. Wang, Voltage-controlled interlayer coupling in perpendicularly magnetized magnetic tunnel junctions. *Nat. Commun.* **8**, 15232 (2017).

19. D. L. Zhang, M. Bapna, W. Jiang, D. Sousa, Y. C. Liao, Z. Y. Zhao, Y. Lv, P. Sahu, D. Y. Lyu, A. Naeemi, T. Low, S. A. Majetich, J. P. Wang, Bipolar electric-field switching of perpendicular magnetic tunnel junctions through voltage-controlled exchange coupling. *Nano Lett.* **22**, 622–629 (2022).

20. A. A. Khan, J. Schmalhorst, A. Thomas, O. Schebaum, G. Reiss, Dielectric breakdown in Co-Fe-B/MgO/Co-Fe-B magnetic tunnel junction. *J. Appl. Phys.* **103**, 123705 (2008).

21. Y. Kato, H. Yoda, Y. Saito, S. Oikawa, K. Fujii, M. Yoshiki, K. Koi, H. Sugiyama, M. Ishikawa, T. Inokuchi, N. Shimomura, M. Shimizu, S. Shirotori, B. Altansargai, Y. Ohsawa, K. Ikegami, A. Tiwari, A. Kurobe, Giant voltage-controlled magnetic anisotropy effect in a crystallographically strained CoFe system. *Appl. Phys. Exp.* **11**, 053007 (2018).

22. T. Nozaki, A. Kozioł-Rachwał, M. Tsujikawa, Y. Shiota, X. D. Xu, T. Ohkubo, T. Tsukahara, S. Miwa, M. Suzuki, S. Tamaru, H. Kubota, A. Fukushima, K. Hono, M. Shirai, Y. Suzuki, S. Yuasa, Highly efficient voltage control of spin and enhanced interfacial perpendicular magnetic anisotropy in iridium-doped Fe/MgO magnetic tunnel junctions. *NPG Asia Mater.* **9**, e451 (2017).

23. T. Nozaki, M. Endo, M. Tsujikawa, T. Yamamoto, T. Nozaki, M. Konoto, H. Ohmori, Y. Higo, H. Kubota, A. Fukushima, M. Hosomi, M. Shirai, Y. Suzuki, S. Yuasa, Voltage-controlled magnetic anisotropy in an ultrathin Ir-doped Fe layer with a CoFe termination layer. *APL Mater.* **8**, 011108 (2020).

24. T. Nozaki, T. Yamamoto, S. Tamaru, H. Kubota, A. Fukushima, Y. Suzuki, S. Yuasa, Enhancement in the interfacial perpendicular magnetic anisotropy and the voltage-controlled magnetic anisotropy by heavy metal doping at the Fe/MgO interface. *APL Mater.* **6**, 026101 (2018).

25. W. Eerenstein, N. D. Mathur, J. F. Scott, Multiferroic and magnetoelectric materials. *Nature* **442**, 759–765 (2006).

26. M. Fiebig, T. Lottermoser, D. Meier, M. Trassin, The evolution of multiferroics. *Nat. Rev. Mater.* **1**, 16046 (2016).

27. C. W. Nan, M. I. Bichurin, S. X. Dong, D. Viehland, G. Srinivasan, Multiferroic magnetoelectric composites: Historical perspective, status, and future directions. *J. Appl. Phys.* **103**, 031101 (2008).

28. M. Fiebig, Revival of the magnetoelectric effect. *J. Phys. D Appl. Phys.* **38**, R123–R152 (2005).

29. M. Gajek, M. Bibes, S. Fusil, K. Bouzehouane, J. Fontcuberta, A. Barthélémy, A. Fert, Tunnel junctions with multiferroic barriers. *Nat. Mater.* **6**, 296–302 (2007).

30. V. Garcia, M. Bibes, L. Bocher, S. Valencia, F. Kronast, A. Crassous, X. Moya, S. Enouz-Vedrenne, A. Gloter, D. Imhoff, C. Deranlot, N. D. Mathur, S. Fusil, K. Bouzehouane, A. Barthélémy, Ferroelectric control of spin polarization. *Science* **327**, 1106–1110 (2010).

31. D. Pantel, S. Goetze, D. Hesse, M. Alexe, Reversible electrical switching of spin polarization in multiferroic tunnel junctions. *Nat. Mater.* **11**, 289–293 (2012).

32. J. Pawlak, W. Skowroński, A. Żywczak, M. Przybylski, Room-temperature multiferroicity and magnetization dynamics in Fe/BTO/LSMO tunnel junction. *Adv. Electron. Mater.* **8**, 2100574 (2022).

33. P. S. Li, A. T. Chen, D. L. Li, Y. G. Zhao, S. Zhang, L. F. Yang, Y. Liu, M. H. Zhu, H. Y. Zhang, X. F. Han, Electric field manipulation of magnetization rotation and tunneling magnetoresistance of magnetic tunnel junctions at room temperature. *Adv. Mater.* **26**, 4320–4325 (2014).

34. A. T. Chen, Y. Wen, B. Fang, Y. L. Zhao, Q. Zhang, Y. S. Chang, P. S. Li, H. Wu, H. L. Huang, Y. L. Lu, Z. M. Zeng, J. W. Cai, X. F. Han, T. Wu, X. X. Zhang, Y. G. Zhao, Giant nonvolatile manipulation of magnetoresistance in magnetic tunnel junctions by electric fields via magnetoelectric coupling. *Nat. Commun.* **10**, 243 (2019).

35. A. T. Chen, Y. L. Zhao, Y. Wen, L. Pan, P. S. Li, X. X. Zhang, Full voltage manipulation of the resistance of a magnetic tunnel junction. *Sci. Adv.* **5**, eaay5141 (2019).

36. Y. J. Yang, Z. L. Luo, S. T. Wang, W. Y. Huang, G. L. Wang, C. M. Wang, Y. X. Yao, H. J. Li, Z. L. Wang, J. T. Zhou, Y. Q. Dong, Y. Guan, Y. C. Tian, C. Feng, Y. G. Zhao, C. Gao, G. Xiao, Electric-field-assisted non-volatile magnetic switching in a magnetoelectronic hybrid structure. *iScience*. **24**, 102734 (2021).

37. Z. Y. Zhao, M. Jamali, N. D'Souza, D. L. Zhang, S. Bandyopadhyay, J. Atulasimha, J. P. Wang, Giant voltage manipulation of MgO-based magnetic tunnel junctions via localized anisotropic strain: A potential pathway to ultra-energy-efficient memory technology. *Appl. Phys. Lett.* **109**, 092403 (2016).

38. A. T. Chen, H. G. Piao, M. H. Ji, B. Fang, Y. Wen, Y. Ma, P. Li, X.-X. Zhang, Using dipole interaction to achieve nonvolatile voltage control of magnetism in multiferroic heterostructures. *Adv. Mater.* **33**, e2105902 (2021).

39. S. Zhang, Y. G. Zhao, P. S. Li, J. J. Yang, S. Rizwan, J. X. Zhang, J. Seidel, T. L. Qu, Y. J. Yang, Z. L. Luo, Q. He, T. Zou, Q. P. Chen, J. W. Wang, L. F. Yang, Y. Sun, Y. Z. Wu, X. Xiao, X. F. Jin, J. Huang, C. Gao, X. F. Han, R. Ramesh, Electric-field control of nonvolatile magnetization in $Co_{40}Fe_{40}B_{20}/Pb(Mg_{1/3}Nb_{2/3})_{0.7}$ $Ti_{0.3}O_3$ Structure at room temperature. *Phys. Rev. Lett.* **108**, 137203 (2012).

40. T. Wu, A. Bur, P. Zhao, K. P. Mohanchandra, K. Wong, K. L. Wang, C. S. Lynch, G. P. Carman, Giant electric-field-induced reversible and permanent magnetization reorientation on magnetoelectric Ni/(011) $[Pb(Mg_{1/3}Nb_{2/3})O_3]_{(1-x)}$-$[PbTiO_3]_x$ heterostructure. *Appl. Phys. Lett.* **98**, 012504 (2011).

41. Z. Wang, Y. Wang, W. Ge, J. Li, D. Viehland, Volatile and nonvolatile magnetic easy-axis rotation in epitaxial ferromagnetic thin films on ferroelectric single crystal substrates. *Appl. Phys. Lett.* **103**, 132909 (2013).

42. G. Q. Yu, Z. X. Wang, M. Abolfath-Beygi, C. L. He, X. Li, K. L. Wong, P. Nordeen, H. Wu, G. P. Carman, X. F. Han, I. A. Alhomoudi, P. K. Amiri, K. L. Wang, Strain-induced modulation of perpendicular magnetic anisotropy in Ta/CoFeB/MgO structures investigated by ferromagnetic resonance. *Appl. Phys. Lett.* **106**, 072402 (2015).

43. B. Peng, Z. Y. Zhou, T. X. Nan, G. H. Dong, M. M. Feng, Q. Yang, X. J. Wang, S. S. Zhao, D. Xian, Z. D. Jiang, W. Ren, Z. G. Ye, N. X. Sun, M. Liu, Deterministic switching of perpendicular magnetic anisotropy by voltage control of spin reorientation transition in

$(Co/Pt)_3/Pb(Mg_{1/3}Nb_{2/3})O_3$–$PbTiO_3$ Multiferroic heterostructures. *ACS Nano* **11**, 4337–4345 (2017).

44. Y. Sun, Y. Ba, A. T. Chen, W. He, W. B. Wang, X. L. Zheng, L. K. Zou, Y. J. Zhang, Q. Yang, L. J. Yan, C. Feng, Q. H. Zhang, J. W. Cai, W. D. Wu, M. Liu, L. Gu, Z. H. Cheng, C. W. Nan, Z. Q. Qiu, Y. Z. Wu, J. Li, Y. G. Zhao, Electric-field modulation of interface magnetic anisotropy and spin reorientation transition in $(Co/Pt)_3$/PMN-PT heterostructure. *ACS Appl. Mater. Interfaces* **9,** 10855–10864 (2017).

45. S. Bhatti, R. Sbiaa, A. Hirohata, H. Ohno, S. Fukami, S. N. Piramanayagam, Spintronics based random access memory: A review. *Mater. Today* **20**, 530–548 (2017).

46. B. Dieny, I. L. Prejbeanu, K. Garello, P. Gambardella, P. Freitas, R. Lehndorff, W. Raberg, U. Ebels, S. O. Demokritov, J. Akerman, A. Deac, P. Pirro, C. Adelmann, A. Anane, A. V. Chumak, A. Hirohata, S. Mangin, S. O. Valenzuela, M. C. Onbaşlı, M. d'Aquino, G. Prenat, G. Finocchio, L. Lopez-Diaz, R. Chantrell, O. Chubykalo-Fesenko, P. Bortolotti, Opportunities and challenges for spintronics in the microelectronics industry. *Nat. electron.* **3**, 446–459 (2020)

47. B. M. S. Teixeira, A. A. Timopheev, N. Caçoilo, S. Auffret, R. C. Sousa, B. Dieny, N. A. Sobolev, Stabilization of the easy-cone magnetic state in free layers of magnetic tunnel junctions. *Phys. Rev. B* **100**, 184405 (2019).

48. A. A. Timopheev, R. Sousa, M. Chshiev, H. T. Nguyen, B. Dieny, Second order anisotropy contribution in perpendicular magnetic tunnel junctions. *Sci. Rep.* **6**, 26877 (2016).

49. A. Atitoaie, I. Firastrau, L. D. Buda-Prejbeanu, U. Ebels, M. Volmer, Macrospin analysis of RF excitations within fully perpendicular magnetic tunnel junctions with second order easy-axis magnetic anisotropy contribution. *J. Appl. Phys.* **124**, 093902 (2018).

50. H. Sato, M. Yamanouchi, S. Ikeda, S. Fukami, F. Matsukura, H. Ohno, Perpendicular-anisotropy CoFeB-MgO magnetic tunnel junctions with a MgO/CoFeB/Ta/CoFeB/MgO recording structure. *Appl. Phys. Lett.* **101**, 022414 (2012).

51. M. X. Wang, W. L. Cai, K. H. Cao, J. Q. Zhou, J. Wrona, S. Z. Peng, H. W. Yang, J. Q. Wei, W. Kang, Y. G. Zhang, J. Langer, B. Ocker, A. Fert, W. S. Zhao, Current-induced magnetization switching in atom-thick tungsten engineered perpendicular magnetic tunnel junctions with large tunnel magnetoresistance. *Nat. Commun.* **9**, 671 (2018).

52. P. Khanal, B. W. Zhou, M. Andrade, Y. L. Dang, A. Davydov, A. Habiboglu, J. Saidian, A. Laurie, J. P. Wang, D. B Gopman, W. G. Wang, Perpendicular magnetic tunnel junctions with multi-interface free layer. *Appl. Phys. Lett.* **119**, 242404 (2021).

53. O. Bultynck, M. Manfrini, A. Vaysset, J. Swerts, C. J. Wilson, B. Sorée, M. Heyns, D. Mocuta, I. P. Radu, T. Devolder, Instant-on spin torque in noncollinear magnetic tunnel junctions. *Phys. Rev. Appl.* **10**, 054028 (2018).

54. C. Safranski, J. Z. Sun, Interface moment dynamics and its contribution to spin-transfer torque switching process in magnetic tunnel junctions. *Phys. Rev. B* **100**, 014435 (2019).

55. G. C. Han, K. Y. Zhang, X. L. Yang, L. B. Ai, M. Wang, B. Liu, Magnetic switching behavior of each magnetic layer in perpendicular magnetic tunnel junctions. *J. Magn. Magn. Mater.* **527**, 167789 (2021).

56. J. C. Slonczewski, Conductance and exchange coupling of two ferromagnets separated by a tunneling barrier. *Phys. Rev. B* **39**, 6995 (1989), 7002.

57. H. J. A. Molegraaf, J. Hoffman, C. A. F. Vaz, S. Gariglio, D. van der Marel, C. H. Ahn, J. M. Triscone, Magnetoelectric effects in complex oxides with competing ground states. *Adv. Mater.* **21**, 3470–3474 (2009).

58. C. A. F. Vaz, Electric field control of magnetism in multiferroic heterostructures. *J. Phys. Condens. Matter* **24**, 333201 (2012).

59. D. Pesquera, E. Khestanova, M. Ghidini, S. Zhang, A. P. Rooney, F. Maccherozzi, P. Riego, S. Farokhipoor, J. Kim, X. Moya, M. E. Vickers, N. A. Stelmashenko, S. J. Haigh, S. S. Dhesi, N. D. Mathur, Large magnetoelectric coupling in multiferroic oxide heterostructures assembled via epitaxial lift-off. *Nat. Commun.* **11**, 3190 (2020).

60. W. H. Liang, F. X. Hu, J. Zhang, H. Kuang, J. Li, J. F. Xiong, K. M. Qiao, J. Wang, J. R. Sun, B. G. Shen, Anisotropic nonvolatile magnetization controlled by electric field in amorphous SmCo thin films grown on (011)-cut PMN-PT substrates. *Nanoscale* **11**, 246–257 (2019).

61. M. Liu, T. X. Nan, J. M. Hu, S. S. Zhao, Z. Y. Zhou, C. Y. Wang, Z. D. Jiang, W. Ren, Z. G. Ye, L. Q. Chen, N. X. Sun, Electrically controlled non-volatile switching of magnetism in multiferroic heterostructures via engineered ferroelastic domain states. *NPG Asia Materials* **8**, e316 (2016).

62. C. Feng, Y. Liu, H. L. Huang, Z. Z. Zhu, Y. J. Yang, Y. Ba, S. Y. Yan, J. W. Cai, Y. L. Lu, J. X. Zhang, S. Zhang, Y. G. Zhao, Unusual behaviors of electric-field control of magnetism in multiferroic heterostructures via multifactor cooperation. *ACS Appl. Mater. Interfaces* **11**, 25569–25577 (2019).

63. B. Noheda, Phase diagram of the ferroelectric relaxor $(1-x)PbMg_{1/3}Nb_{2/3}O_3-xPbTiO_3$. *Phys. Rev. B* **66**, 054104 (2002).

64. G. Vinai, F. Motti, V. Bonanni, A. Y. Petrov, S. Benedetti, C. Rinaldi, M. Stella, D. Cassese, S. Prato, M. Cantoni, G. Rossi, G. Panaccione, P. Torelli, Reversible modification of ferromagnetism through electrically controlled morphology. *Adv. Electron. Mater.* **5**, 1900150 (2019).

65. S. H. Baek, H. W. Jang, C. M. Folkman, Y. L. Li, B. Winchester, J. X. Zhang, Q. He, Y. H. Chu, C. T. Nelson, M. S. Rzchowski, X. Q. Pan, R. Ramesh, L. Q. Chen, C. B. Eom, Ferroelastic switching for nanoscale non-volatile magnetoelectric devices. *Nat. Mater.* **9**, 309–314 (2010).

66. M. Liu, B. M. Howe, L. Grazulis, K. Mahalingam, T. X. Nan, N. X. Sun, G. J. Brown, Voltage-impulse-induced non-volatile ferroelastic switching of ferromagnetic resonance for reconfigurable magnetoelectric microwave Devices. *Adv. Mater.* **25**, 4886–4892 (2013).

67. J. Wang, D. Pesquera, R. Mansell, S. van Dijken, R. P. Cowburn, M. Ghidini, N. D. Mathu, Giant non-volatile magnetoelectric effects via growth anisotropy in $Co_{40}Fe_{40}B_{20}$ films on PMN-PT substrates. *Appl. Phys. Lett.* **114**, 092401 (2019).

68. P. Wang, C. Jin, Y. C. Wang, S. S. Liu, X. Y. Wang, D. X. Zheng, W. C. Zheng, H. L. Bai, Differentiation of non-volatile strain and ferroelectric field effects in (011)- and (001)-$La_{0.67}Sr_{0.33}MnO_3/Pb(Mg_{1/3}Nb_{2/3})_{0.7}Ti_{0.3}O_3$ heterostructures. *J. Appl. Phys.* **127**, 244102 (2020).

69. S. H. Baek, J. Park, D. M. Kim, V. A. Aksyuk, R. R. Das, S. D. Bu, D. A. Felker, J. Lettieri, V. Vaithyanathan, S. S. N. Bharadwaja, N. Bassiri-Gharb, Y. B. Chen, H. P. Sun, C. M. Folkman, H. W. Jang, D. J. Kreft, S. K. Streiffer, R. Ramesh, X. Q. Pan, S. Trolier-McKinstry, D. G. Schlom, M. S. Rzchowski, R. H. Blick, C. B. Eom, Giant piezoelectricity on Si for hyperactive MEMS. *Science* **334**, 958–961 (2011).

70. J. Irwin, S. Lindemann, W. Maeng, J. J. Wang, V. Vaithyanathan, J. M. Hu, L. Q. Chen, D. G. Schlom, C. B. Eom, M. S. Rzchowski, Magnetoelectric coupling by piezoelectric tensor design. *Sci. Rep.* **9**, 19158 (2019).

71. S. Lindemann, J. Irwin, G. Y. Kim, B. Wang, K. Eom, J. J. Wang, J. M. Hu, L. Q. Chen, S. Y. Choi, C. B. Eom, M. S. Rzchowski, Low-voltage magnetoelectric coupling in membrane heterostructures. *Sci. Adv.* **7**, eabh2294 (2021).

72. R. C. Peng, J. M. Hu, K. Momeni, J. J. Wang, L. Q. Chen, C. W. Nan, Fast 180° magnetization switching in a strain-mediated multiferroic heterostructure driven by a voltage. *Sci. Rep.* **6**, 27561 (2016).

73. N. Locatelli, V. Cros, Basic spintronic transport phenomena, in *Introduction to Magnetic Random-Access Memory*, B. Dieny, R. B. Goldfarb, K. J. Lee, Eds. (Wiley, 2017), chap. 1.

74. L. F. Yang, Y. G. Zhao, S. Zhang, P. S. Li, Y. Gao, Y. J. Yang, H. L. Huang, P. X. Miao, Y. Liu, A. T. Chen, C. W. Nan, C. Gao, Bipolar loop-like non-volatile strain in the (001)-oriented $Pb(Mg_{1/3}Nb_{2/3})O_3$-$PbTiO_3$ single crystals. *Sci. Rep.* **4**, 4591 (2014).

75. M. Birkholz, "Principles of x-ray diffraction, in *Thin Film Analysis by X-Ray Scattering*, M. Birkholz, Ed. (Weinheim, 2006), chap. 1.